Journal of Computational Physics **177,** 336–364 (2002)
doi:10.1006/jcph.2002.7012, available online at http://www.idealibrary.com on IDEAL®

Analysis of a Fractional-Step Method on Overset Grids

Tristan M. Burton and John K. Eaton

Mechanical Engineering Department, Stanford University, Stanford, California 94305-3030
E-mail: tburton@snarf.stanford.edu

Received January 18, 2001; revised September 14, 2001

A fractional-step method for solving the incompressible Navier–Stokes equations on overset grids is derived as a matrix factorization of the spatially and temporally discretized system of equations. The algorithm is applied to several test problems using second-order-accurate finite-volume flux differencing on staggered grid systems and a hybrid implicit/explicit time advancement scheme. Spatial order of accuracy is shown to depend on the behavior of the overset grid overlap during grid refinement. The temporal order of accuracy of the time advancement algorithm on a single grid is maintained on the overset grid. © 2002 Elsevier Science (USA)

Key Words: unsteady Navier–Stokes; fractional-step; overset grids; staggered grid.

1. INTRODUCTION

In complex flow configurations the use of overset grids can simplify considerably the gridding and solution processes. Consider an array of spheres in a box of incompressible turbulence. A single unstructured grid could be used but the gridding procedure would be complex and the grid would need to be regenerated if the spheres were to move. Alternatively, a single Cartesian background grid with overset spherical grids could be used. In this case all the grids are structured and the spheres could move without any modifications to the grid system. A natural decomposition of the problem also occurs with overset grids, which allows for parallel implementation of the solution procedure.

Many authors have used overset grids to solve the unsteady, incompressible Navier–Stokes equations. Kiris *et al*. [7] used artificial compressibility to solve for the flow in artificial heart devices. Tu and Fuchs [16] used a multigrid procedure to solve for the flow in an internal combustion engine with a moving boundary. Other authors have used projection methods where the solution to an elliptic equation is used to update the pressure and enforce the incompressibility constraint. Perng and Street [13] used a predictor–corrector time advancement scheme with a multigrid algorithm for the solution of the pressure equation.

0021-9991/02 $35.00

Hinatsu and Ferziger [6] used a similar numerical technique, but they considered cases where nodes from different component grids did not overlap exactly as in [13]. Closely related to the projection methods is the solution of the velocity–pressure formulation of the Navier–Stokes equations. Henshaw [5] has developed a spatially fourth-order-accurate overset grid method for this formulation.

Here we develop a fractional-step method specifically for the solution of the unsteady, incompressible Navier–Stokes equations on overset grids. The algorithm is developed using an approximate matrix factorization of the spatially and temporally discretized system of equations, as was done by Dukowicz and Dvinsky [4] and Perot [14] for solution of the unsteady, incompressible Navier–Stokes equations on a single grid. The factorization elucidates all details of the coupling between the component grids, including the pressure coupling considered by other authors using pressure projection methods on overset grids [6, 13]. The derivation of the general algorithm is independent of the grid scheme, spatial discretization, and time advancement scheme to ensure a wide range of application.

An important part of the development of any numerical scheme is the validation of the spatial and temporal orders of accuracy. Henshaw [5] has validated the fourth-order spatial accuracy of his overset grid method. However, other authors [6, 13] do not include relevant spatial order of accuracy results. These authors also run time-accurate, fully explicit codes on steady-state problems and thus do not validate the temporal order of accuracy. We wish to compute unsteady problems with a hybrid implicit/explicit time advancement scheme and permit different treatment of terms on different component grids. Therefore, it is important to validate the temporal order of accuracy. We apply our overset grid algorithm to various test problems to show that the predicted spatial and temporal orders of accuracy are maintained.

2. NUMERICAL METHOD

The current work focuses on solving the unsteady, incompressible Navier–Stokes equations in dimensionless form,

$$\frac{\partial \mathbf{u}}{\partial t} + (\mathbf{u} \cdot \nabla)\mathbf{u} = -\nabla p + \frac{1}{Re}\nabla^2 \mathbf{u}, \tag{1}$$

$$\nabla \cdot \mathbf{u} = 0, \tag{2}$$

on an overset grid. An example of an overset grid suitable for solving for the flow in a square domain is shown in Fig. 1. Here we define an overset grid as a combination of component grids where interpolation from another component grid is required on some portion of each component grid boundary to determine the solution. One component grid may completely overlap another, as shown in Fig. 1, or the overlap region may only include some fraction of each of the component grids. Though the overset grid may be composed of an arbitrary number of component grids, a two-grid system is sufficient to demonstrate the matrix factorization that leads to our fractional-step method for overset grids. The fractional-step method on an overset grid composed of more than two component grids is a simple extension of the algorithm derived here. If desired, the matrix factorization can be performed on systems with more than two component grids, but the linear algebra becomes cumbersome.

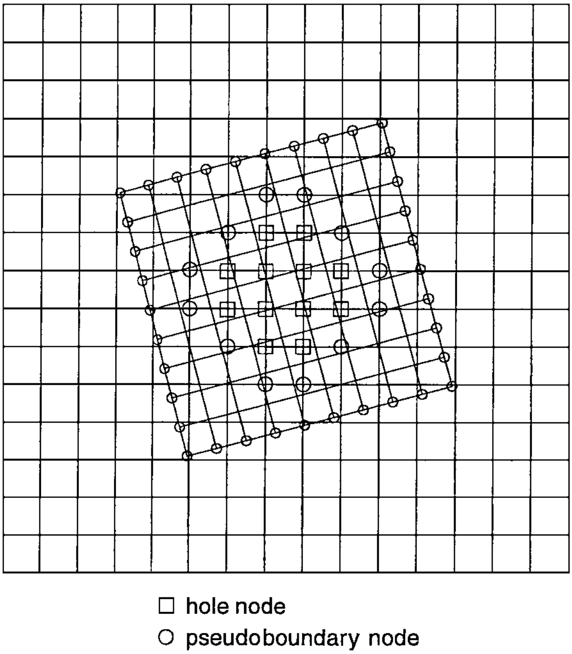

FIG. 1. Sample overset grid system composed of two component grids.

2.1. Single-Grid Method

The derivation of the overset grid fractional-step method is similar to the derivations of single-grid fractional-step methods considered by other authors [4, 9, 14]. In order to simplify the discussion of the overset grid fractional-step method and to help highlight the differences between the single-grid and overset grid solution procedures, we begin by considering the solution of Eqs. (1) and (2) on a single grid.

2.1.1. *Spatial Discretization*

The equations are first discretized in space using the chosen grid scheme and spatial discretization. We can write the spatially discretized equations in matrix form as

$$\frac{\partial \mathbf{u}}{\partial t} = -Gp - G_{bc}p_{bc} + N(\mathbf{u}, \mathbf{u}_{bc}) + M\mathbf{u} + M_{bc}\mathbf{u}_{bc}, \tag{3}$$

$$D\mathbf{u} + D_{bc}\mathbf{u}_{bc} = 0, \tag{4}$$

where $\mathbf{u}$ is the spatially discretized velocity vector and p is the spatially discretized pressure. The spatially discretized velocity and pressure are each split into an unknown part ($\mathbf{u}$ and p) that must be solved for and the part which is a given boundary condition ($\mathbf{u}_{bc}$ and p_{bc}). Because of this splitting, the spatial discretization of the terms in the continuous equations must also be split. The contribution of the viscous terms in Eq. (3) is represented as $M\mathbf{u} + M_{bc}\mathbf{u}_{bc}$, where M and M_{bc} are matrices that contain the spatial discretization information. The contribution of the pressure gradient is written as a pair of matrix–vector products, Gp and $G_{bc}p_{bc}$. Since the nonlinear term cannot be written as a matrix–vector product where

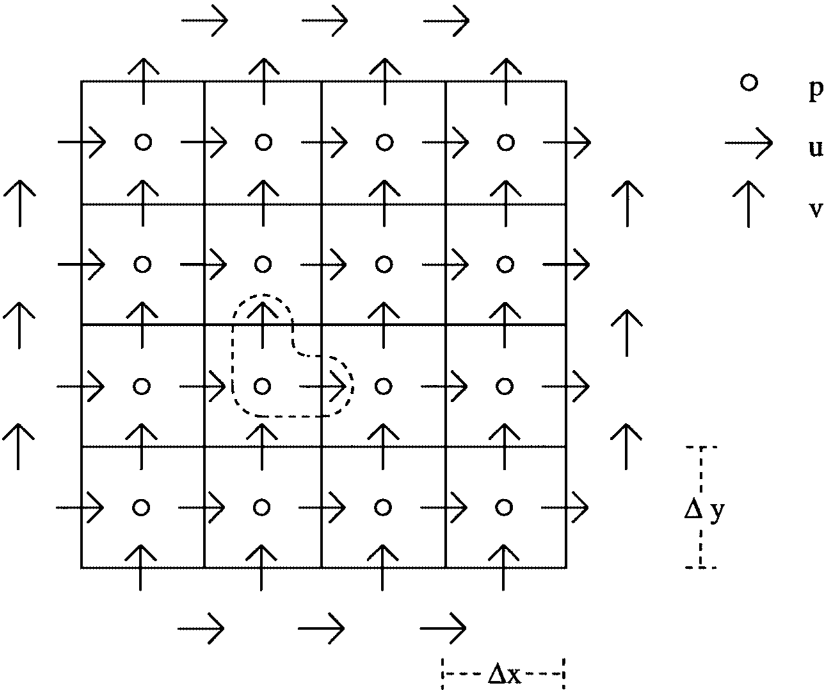

FIG. 2. Two-dimensional staggered grid.

the matrix is independent of the velocity we write it as $N(\mathbf{u}, \mathbf{u}_{bc})$. The discrete continuity equation (4) contains a pair of matrix–vector products.

The terms in Eqs. (3) and (4) depend on the grid scheme and discretization and some of the terms may not be present in all cases. In a problem with periodic boundary conditions, all of the values in the spatially discretized velocity vector and pressure are unknowns and the terms in Eqs. (3) and (4) due to boundary conditions will not appear. If a staggered grid with second-order-accurate differencing is chosen for the spatial discretization, then pressure boundary conditions are not required and the $G_{bc} p_{bc}$ term does not appear in Eq. (3). To help clarify the matrix form of the spatially discretized equations, we consider a second-order spatial discretization of the two-dimensional form of Eqs. (1) and (2) on a uniform staggered grid in a square domain. The grid is shown in Fig. 2. Included in the diagram are the ghost nodes outside the grid that may be required to enforce boundary conditions on the velocity. Here we will assume that the velocity is prescribed at the boundary of the grid. Therefore, the ghost nodes are used so that the tangential component of velocity (computed with a two-point average) obeys the prescribed boundary condition.

For each of the u nodes inside the grid boundary in Fig. 2, the spatially discretized momentum equation is

$$\frac{\partial u_{i,j}}{\partial t} = -\frac{p_{i+1,j} - p_{i,j}}{\Delta x} + \frac{1}{Re}\left(\frac{u_{i+1,j} - 2u_{i,j} + u_{i-1,j}}{\Delta x^2} + \frac{u_{i,j+1} - 2u_{i,j} + u_{i,j-1}}{\Delta y^2}\right)$$
$$- \frac{(uu)_{i+1,j} - (uu)_{i,j}}{\Delta x} - \frac{(uv)_{i,j} - (uv)_{i,j-1}}{\Delta y} \quad \text{for } (i, j) = (1, 1) : (3, 4), \quad (5)$$

and for each of the v nodes inside the grid boundary, the spatially discretized momentum equation is

$$\frac{\partial v_{i,j}}{\partial t} = -\frac{p_{i,j+1} - p_{i,j}}{\Delta y} + \frac{1}{Re}\left(\frac{v_{i+1,j} - 2v_{i,j} + v_{i-1,j}}{\Delta x^2} + \frac{v_{i,j+1} - 2v_{i,j} + v_{i,j-1}}{\Delta y^2}\right) - \frac{(uv)_{i,j} - (uv)_{i-1,j}}{\Delta x} - \frac{(vv)_{i,j+1} - (vv)_{i,j}}{\Delta y} \quad \text{for } (i,\, j) = (1, 1) : (4, 3). \tag{6}$$

The continuity equation is discretized at the location of the pressure nodes and can be written as

$$\frac{u_{i,j} - u_{i-1,j}}{\Delta x} + \frac{v_{i,j} - v_{i,j-1}}{\Delta y} = 0 \quad \text{for } (i,\, j) = (1, 1) : (4, 4). \tag{7}$$

Note that the u velocity node to the right of and the v velocity node above each pressure node have the same $(i,\, j)$ index as the pressure node.

We now can describe the form of the vectors and matrices in Eqs. (3) and (4) for the grid in Fig. 2. The unknown velocity vector, $\mathbf{u}$, has 24 elements and the unknown pressure vector, p, has 16 elements. The velocity boundary condition vector, $\mathbf{u}_{bc}$, has 28 elements, where 16 are due to the boundary condition on the normal component of the velocity and the remaining 12 are due to the boundary condition on the tangential component. The G matrix is of size 24 by 16 and only two elements in any row of the matrix are nonzero. As discussed previously, the G_{bc} term in Eq. (3) does not appear since pressure boundary conditions are not required on a staggered grid. The M matrix is of size 24 by 24 and the M_{bc} matrix is of size 24 by 28. Our second-order discretization of the viscous term in Eqs. (5) and (6) uses a five-point stencil. Therefore, the combined number of nonzero entries in the same row of the M and M_{bc} matrices must be five. If the row corresponds to the equation for a velocity node adjacent to two boundaries, then the M matrix will have three nonzero entries and the M_{bc} matrix will have two nonzero entries. Similarly, all five nonzero entries will appear in the M matrix if the row corresponds to the equation for a velocity node that is not adjacent to a boundary. The form of the discrete nonlinear operator, $N(\mathbf{u}, \mathbf{u}_{bc})$, can be inferred from Eqs. (5) and (6). In Eq. (4), the D matrix is of size 16 by 24 and the D_{bc} matrix is of size 16 by 28. Since the discretized continuity equation (7) uses four velocity nodes, the combined number of nonzero entries in the same row of the D and D_{bc} matrices must be four.

2.1.2. *Temporal Discretization*

After spatial discretization is complete, a temporal discretization scheme is applied to Eqs. (3) and (4). As an example, consider time advancement with third-order Runge–Kutta for the convective terms, Crank–Nicolson for the viscous terms, and implicit Euler for the pressure gradient term. This three-step time advancement scheme [15] can be written as

$$\begin{aligned}[I - \beta_k \Delta t M]\mathbf{u}^k + 2\beta_k \Delta t G \delta p^k &= \mathbf{u}^{k-1} + \beta_k \Delta t\left[M\mathbf{u}^{k-1} + M_{bc}\mathbf{u}_{bc}^{k-1} + M_{bc}\mathbf{u}_{bc}^{k}\right] + \gamma_k \Delta t N\left(\mathbf{u}^{k-1}, \mathbf{u}_{bc}^{k-1}\right) \\ &\quad + \zeta_k \Delta t N\left(\mathbf{u}^{k-2}, \mathbf{u}_{bc}^{k-2}\right) - 2\beta_k \Delta t\left[G p^{k-1} + G_{bc} p_{bc}^{k}\right],\end{aligned} \tag{8}$$

$$D\mathbf{u}^k + D_{bc}\mathbf{u}_{bc}^k = 0, \tag{9}$$

where $k = 1, 2, 3$ is the substep index, $\mathbf{u}^0$ is the solution at the beginning of the time step ($\mathbf{u}^{n-1}$), and $\mathbf{u}^3$ is the solution at the end of the time step ($\mathbf{u}^n$). Note that we have written the unknown pressure term in delta form, where $\delta p^k = p^k - p^{k-1}$. The coefficients for this time advancement scheme are

$$\begin{aligned} \beta_1 &= \frac{4}{15} & \beta_2 &= \frac{1}{15} & \beta_3 &= \frac{1}{6} \\ \gamma_1 &= \frac{8}{15} & \gamma_2 &= \frac{5}{12} & \gamma_3 &= \frac{3}{4} \\ \zeta_1 &= 0 & \zeta_2 &= -\frac{17}{60} & \zeta_3 &= -\frac{5}{12}. \end{aligned} \tag{10}$$

The spatially and temporally discretized system of equations can now be written in a compact, block matrix form as follows:

$$\begin{bmatrix} B & H \\ D & 0 \end{bmatrix} \begin{bmatrix} \mathbf{u}^n \\ \delta p^n \end{bmatrix} = \begin{bmatrix} \mathbf{r}^{n-1} \\ 0 \end{bmatrix} + \begin{bmatrix} bc's \\ bc's \end{bmatrix}. \tag{11}$$

Here we have lumped the contribution to the right hand side from the previously computed solution into one vector, $\mathbf{r}^{n-1}$, and all the boundary condition information into another vector to simplify the notation. Any choice of spatial and temporal discretization of Eqs. (1) and (2) where the nonlinear terms are treated explicitly can be written in the block matrix form of Eq. (11). If the chosen temporal discretization involves multiple substeps to complete a full time step, as in Eq. (8), then Eq. (11) will be solved at each substep.

2.1.3. *Block LU Decomposition*

In order to avoid solving the fully coupled system in Eq. (11), we wish to find an approximate factorization of the matrix on the left hand side. To perform the factorization, we consider a modified version of Eq. (11):

$$\begin{bmatrix} B & BH \\ D & 0 \end{bmatrix} \begin{bmatrix} \mathbf{u}^n \\ \delta p^n \end{bmatrix} = \begin{bmatrix} \mathbf{r}^{n-1} \\ 0 \end{bmatrix} + \begin{bmatrix} bc's \\ bc's \end{bmatrix}. \tag{12}$$

In this new system, the pressure gradient term in the momentum equations has been modified. For the time advancement algorithm in Eq. (8), the new term can be written as $H\delta p^k - 2(\beta_k \Delta t)^2 MG\delta p^k$. This differs from the original term by $\mathcal{O}(\Delta t^3)$ since δp^k is $\mathcal{O}(\Delta t)$. Therefore, the solution of Eq. (12) is equivalent to the solution of Eq. (11) with an extra error term of $\mathcal{O}(\Delta t^3)$ on the right hand side. Since this error term is of the same order as the temporal discretization error associated with Crank–Nicolson time advancement, we maintain the temporal order of accuracy of our solution by solving Eq. (12). Other choices of second-order implicit/explicit time advancement algorithms will produce a similar result.

We perform a block *LU* decomposition of the matrix on the left hand side of Eq. (12):

$$\begin{bmatrix} B & 0 \\ D & -DH \end{bmatrix} \begin{bmatrix} I & H \\ 0 & I \end{bmatrix} \begin{bmatrix} \mathbf{u}^n \\ \delta p^n \end{bmatrix} = \begin{bmatrix} \mathbf{r}^{n-1} \\ 0 \end{bmatrix} + \begin{bmatrix} bc's \\ bc's \end{bmatrix}. \tag{13}$$

Using this *LU* decomposition, we solve Eq. (12) in three steps. First we obtain an intermediate velocity field, $\tilde{\mathbf{u}}^n$:

$$B\tilde{\mathbf{u}}^n = \mathbf{r}^{n-1} + bc's. \tag{14}$$

Next we solve a discrete Poisson equation for the pressure change:

$$DH\delta p^n = D\tilde{\mathbf{u}}^n - bc's. \tag{15}$$

Finally, the solution to the discrete Poisson equation is used to project the intermediate velocity field to a divergence-free subspace:

$$\mathbf{u}^n = \tilde{\mathbf{u}}^n - H\delta p^n. \tag{16}$$

Similar factorizations for systems where both the velocity and pressure unknowns are in delta form were considered by Dukowicz and Dvinsky [4]. Perot [14] has developed approximate factorizations for systems where neither the velocity nor pressure unknowns are in delta form. A more general approach was taken by Lee *et al.* [9], who recently derived all possible exact and approximate factorizations of the matrix on the left hand side of Eq. (11) that lead to useful fractional-step algorithms. A common conclusion reached by all these authors who use approximate factorization to derive fractional-step algorithms is that while the second-order temporal accuracy of the solution of the velocity field can be maintained, the pressure is only first-order accurate in time. While approximate factorization of the fully discretized system of equations is an easy way to develop fractional-step algorithms, it is also possible to perform a time splitting on the semidiscrete version of the Navier–Stokes equations where only the time is discretized. While there are drawbacks to this approach [14], Brown *et al.* [1] have recently shown results from fractional-step algorithms derived in this way that indicate that the pressure can be second-order accurate in time.

2.1.4. *Temporal Order of Accuracy of the Pressure*

We now perform analysis to investigate the temporal order of accuracy of the computed pressure for our fractional-step algorithm using the time advancement algorithm in Eq. (8). Similar analyses can be done for other time advancement algorithms. At each substep, the intermediate velocity field is determined from the solution of

$$\begin{aligned}[I - \beta_k \Delta t M]\tilde{\mathbf{u}}^k = {} & \mathbf{u}^{k-1} + \beta_k \Delta t\left[M\mathbf{u}^{k-1} + M_{bc}\mathbf{u}_{bc}^{k-1} + M_{bc}\mathbf{u}_{bc}^{k}\right] \\ & + \gamma_k \Delta t N\left(\mathbf{u}^{k-1}, \mathbf{u}_{bc}^{k-1}\right) + \zeta_k \Delta t N\left(\mathbf{u}^{k-2}, \mathbf{u}_{bc}^{k-2}\right) \\ & - 2\beta_k \Delta t\left[Gp^{k-1} + G_{bc}p_{bc}^{k}\right].\end{aligned} \tag{17}$$

This equation can then be rewritten using the appropriate form of Eq. (16):

$$\begin{aligned}\tilde{\mathbf{u}}^k = {} & \mathbf{u}^{k-1} + \beta_k \Delta t\left[M\mathbf{u}^{k-1} + M_{bc}\mathbf{u}_{bc}^{k-1} + M\mathbf{u}^k + M_{bc}\mathbf{u}_{bc}^{k}\right] \\ & + \gamma_k \Delta t N\left(\mathbf{u}^{k-1}, \mathbf{u}_{bc}^{k-1}\right) + \zeta_k \Delta t N\left(\mathbf{u}^{k-2}, \mathbf{u}_{bc}^{k-2}\right) \\ & - 2\beta_k \Delta t\left[Gp^{k-1} + G_{bc}p_{bc}^{k}\right] + 2(\beta_k \Delta t)^2 MG\delta p^k.\end{aligned} \tag{18}$$

The discrete Poisson equation that is solved for the pressure change at each substep is

$$DG\delta p^k = \frac{D\tilde{\mathbf{u}}^k + D_{bc}\mathbf{u}_{bc}^k}{2\beta_k \Delta t}. \tag{19}$$

Using Eq. (18) we can now substitute for the intermediate velocity in the discrete Poisson equation for the pressure change and derive the equivalent discrete Poisson equation for the pressure, p^k:

$$\begin{aligned} DGp^k = D\Bigg[&\frac{1}{2}\left(M\mathbf{u}^{k-1} + M_{bc}\mathbf{u}_{bc}^{k-1} + M\mathbf{u}^k + M_{bc}\mathbf{u}_{bc}^k\right) + \frac{\gamma_k}{2\beta_k}N\left(\mathbf{u}^{k-1}, \mathbf{u}_{bc}^{k-1}\right) \\ &+ \frac{\zeta_k}{2\beta_k}N\left(\mathbf{u}^{k-2}, \mathbf{u}_{bc}^{k-2}\right) - G_{bc}p_{bc}^k + \beta_k \Delta t M G \delta p^k\Bigg] + D\left[\frac{\mathbf{u}^{k-1}}{2\beta_k \Delta t}\right] + D_{bc}\left[\frac{\mathbf{u}_{bc}^k}{2\beta_k \Delta t}\right]. \end{aligned} \tag{20}$$

Using the discrete continuity equation (9), we consider Eq. (20) for the third substep since it is the pressure at the end of the time step:

$$\begin{aligned} DGp^3 = D\Bigg[&\frac{1}{2}\left(M\mathbf{u}^2 + M_{bc}\mathbf{u}_{bc}^2 + M\mathbf{u}^3 + M_{bc}\mathbf{u}_{bc}^3\right) + \frac{\gamma_3}{2\beta_3}N\left(\mathbf{u}^2, \mathbf{u}_{bc}^2\right) \\ &+ \frac{\zeta_3}{2\beta_3}N\left(\mathbf{u}^1, \mathbf{u}_{bc}^1\right) - G_{bc}p_{bc}^3 + \beta_3 \Delta t M G \delta p^3\Bigg] + D_{bc}\left[\frac{\mathbf{u}_{bc}^3 - \mathbf{u}_{bc}^2}{2\beta_3 \Delta t}\right]. \end{aligned} \tag{21}$$

We now perform a Taylor series expansion in time about t^3 for the terms on the right hand side of Eq. (21):

$$\begin{aligned} DGp^3 = D\Bigg[&M\mathbf{u}^3 + M_{bc}\mathbf{u}_{bc}^3 - \beta_3 \Delta t\left(\frac{\partial M\mathbf{u}}{\partial t} + \frac{\partial M_{bc}\mathbf{u}_{bc}}{\partial t}\right)\Bigg|_{t_3} \\ &+ \left(\frac{\gamma_3}{2\beta_3} + \frac{\zeta_3}{2\beta_3}\right)N\left(\mathbf{u}^3, \mathbf{u}_{bc}^3\right) - \left(\gamma_3 + \frac{\zeta_3(\beta_2 + \beta_3)}{\beta_3}\right)\Delta t \frac{\partial N(\mathbf{u}, \mathbf{u}_{bc})}{\partial t}\Bigg|_{t_3} \\ &- G_{bc}p_{bc}^3 + \mathcal{O}(\Delta t^2)\Bigg] + D_{bc}\left[\frac{\partial \mathbf{u}_{bc}}{\partial t}\bigg|_{t^3} - \beta_3 \Delta t \frac{\partial^2 \mathbf{u}_{bc}}{\partial t^2}\bigg|_{t^3} + \mathcal{O}(\Delta t^2)\right]. \end{aligned} \tag{22}$$

The continuous time equation for *DGp* is derived by multiplying Eq. (3) by the *D* matrix and using the time derivative of Eq. (4):

$$DGp = D[M\mathbf{u} + M_{bc}\mathbf{u}_{bc} + N(\mathbf{u}, \mathbf{u}_{bc}) - G_{bc}p_{bc}] + D_{bc}\frac{\partial \mathbf{u}_{bc}}{\partial t}. \tag{23}$$

Note that this equation is not necessarily consistent with a discretization of the equation for the pressure that is derived by performing a similiar sequence of operations on the spatially continuous equations:

$$\nabla^2 p = -\nabla \cdot (\mathbf{u} \cdot \nabla \mathbf{u}). \tag{24}$$

At no point in the approximate factorization derivation of fractional-step methods is a spatially continuous Poisson equation discretized in space. The discrete Poisson equation is a by-product of the approximate factorization of the spatially and temporally discretized incompressible Navier–Stokes equation. Attempts to compare the calculated pressure from an approximate factorization fractional-step method to a spatially discretized version of Eq. (24) appear to be misdirected. If a numerical solution for the pressure that obeys a discretization of Eq. (24) (and the associated boundary conditions) is desired, then the velocity–pressure formulation of the Navier–Stokes equations should be used instead of the velocity–divergence formulation.

Using the coefficients in Eq. (10) and comparing Eq. (22) and Eq. (23) we see that the source terms agree to first order in time. Therefore, our computed pressure will be first-order accurate in time. Attempts to improve the time accuracy of the pressure in situations where Eq. (23) is not consistent with a discretized version of Eq. (24) are not useful since the computed pressure may not obey the correct boundary conditions and therefore cannot be used for evaluating flow quantities of interest. Of course, a temporally second-order-accurate pressure that obeys the correct boundary conditions can be obtained at any point in time by using the temporally second-order-accurate velocity components in a discretization of Eq. (24).

In situations where Eq. (23) is consistent with a discretization of Eq. (24), higher order temporal accuracy in the pressure is desirable. Here we perform an analysis to see if the computed pressure can be made second-order accurate in time by using Crank–Nicolson for the time integration of the pressure gradient term in the spatially discretized momentum equations. The discrete Poisson equation for the pressure at t^3 can be written by combining the discrete Poisson equations for the pressure change at each of the three substeps:

$$\begin{aligned} DGp^3 = D\bigg[& M\mathbf{u}^0 + M_{bc}\mathbf{u}^0_{bc} + M\mathbf{u}^3 + M_{bc}\mathbf{u}^3_{bc} - G_{bc}p^0_{bc} - G_{bc}p^3_{bc} \\ & + \left(\frac{\gamma_1}{\beta_1} - \frac{\zeta_2}{\beta_2}\right) N\left(\mathbf{u}^0, \mathbf{u}^0_{bc}\right) + \left(\frac{\zeta_3}{\beta_3} - \frac{\gamma_2}{\beta_2}\right) N\left(\mathbf{u}^1, \mathbf{u}^1_{bc}\right) + \frac{\gamma_3}{\beta_3} N\left(\mathbf{u}^2, \mathbf{u}^2_{bc}\right) \\ & + \beta_1 \Delta t MG\delta p^1 - \beta_2 \Delta t MG\delta p^2 + \beta_3 \Delta t MG \delta p^3 \bigg] - DGp^0 \\ & + D_{bc}\left[\frac{\mathbf{u}^1_{bc} - \mathbf{u}^0_{bc}}{\beta_1 \Delta t} - \frac{\mathbf{u}^2_{bc} - \mathbf{u}^1_{bc}}{\beta_2 \Delta t} + \frac{\mathbf{u}^3_{bc} - \mathbf{u}^2_{bc}}{\beta_3 \Delta t}\right]. \end{aligned} \tag{25}$$

If we assume that the pressure at the beginning of the time step obeys Eq. (23) then we can rewrite Eq. (25) using a Taylor series expansion in time about t^0:

$$\begin{aligned} DGp^3 = D\bigg[& M\mathbf{u}^3 + M_{bc}\mathbf{u}^3_{bc} - G_{bc}p^3_{bc} + \left(\frac{\gamma_1}{\beta_1} - \frac{\gamma_2}{\beta_2} + \frac{\gamma_3}{\beta_3} - \frac{\zeta_2}{\beta_2} + \frac{\zeta_3}{\beta_3} - 1\right) N(\mathbf{u}, \mathbf{u}_{bc})|_{t^0} \\ & + 2\Delta t \left(\beta_1\left(\frac{\zeta_3}{\beta_3} - \frac{\gamma_2}{\beta_2}\right) + (\beta_1 + \beta_2)\frac{\gamma_3}{\beta_3}\right) \frac{\partial N(\mathbf{u}, \mathbf{u}_{bc})}{\partial t}\bigg|_{t^0} + \mathcal{O}(\Delta t^2)\bigg] \\ & + D_{bc}\left[\frac{\partial \mathbf{u}_{bc}}{\partial t}\bigg|_{t^0} + 2\Delta t(\beta_1 + \beta_2 + \beta_3)\frac{\partial^2 \mathbf{u}_{bc}}{\partial t^2}\bigg|_{t_0} + \mathcal{O}(\Delta t^2)\right]. \end{aligned} \tag{26}$$

Using the coefficients in Eq. (10) and comparing to Eq. (23), we see that the source terms agree to first order in time due to the nonlinear term Taylor series expansion. The source terms can be made to agree to second order in time by choosing coefficients for the three-step time advancement algorithm such that

$$\begin{aligned}
&\frac{\gamma_1}{\beta_1} - \frac{\gamma_2}{\beta_2} + \frac{\gamma_3}{\beta_3} - \frac{\zeta_2}{\beta_2} + \frac{\zeta_3}{\beta_3} - 1 = 1 \\
&\beta_1\left(\frac{\zeta_3}{\beta_3} - \frac{\gamma_2}{\beta_2}\right) + (\beta_1 + \beta_2)\frac{\gamma_3}{\beta_3} = \frac{1}{2}.
\end{aligned} \tag{27}$$

A new set of coefficients that obey the constraints in Eq. (27) are

$$\begin{aligned}
&\beta_1 = \frac{4}{15} \quad \beta_2 = \frac{1}{15} \qquad \beta_3 = \frac{1}{6} \\
&\gamma_1 = \frac{8}{15} \quad \gamma_2 = \frac{5}{28} \qquad \gamma_3 = \frac{143}{84} \\
&\zeta_1 = 0 \qquad \zeta_2 = -\frac{19}{420} \quad \zeta_3 = -\frac{115}{84}.
\end{aligned} \tag{28}$$

Unfortunately, these new coefficients reduce the explicit term time advancement scheme to second-order temporal accuracy. However, the Crank–Nicolson treatment of the viscous terms limits the temporal order of accuracy to second order and so the loss of time accuracy in the explicit scheme is not significant. The stability regions for the explicit schemes from the two sets of coefficients are almost identical.

We have shown that it is possible to achieve second-order temporal accuracy for the computed pressure by using Crank–Nicolson for the time integration of the pressure gradient term and modifying the coefficients of the three-step time advancement algorithm. However, this treatment of the pressure gradient term can lead to numerical difficulties due to oscillations in the pressure field [14]. In addition, the discretizations we consider here make Eq. (23) inconsistent with a discretization of Eq. (24), so temporally higher order accurate pressure is not useful. Therefore, we use implicit Euler treatment for the pressure in this work.

2.2. Overset Grid Method Development

The spatial and temporal discretization (with explicit treatment of the nonlinear terms) of the incompressible Navier–Stokes equations on an overset grid composed of two component grids leads to a system of algebraic equations $A\mathbf{x} = \mathbf{b}$ shown in Eq. (29). The dependent variables that make up the solution vector, $\mathbf{x}$, are the velocity vector, $\mathbf{u}^n$, and the pressure change, $\delta p^n = p^n - p^{n-1}$, for each component grid, where the numerical subscripts denote the component grid index. As was the case for the single-grid algorithm, the solution vector in Eq. (29) only contains unknown velocity or pressure nodes in the interior of the domain while the influence of boundary conditions appears on the right hand side. The system matrix, A, is composed of several different submatrices. The C and E submatrices contain interpolation weights for the velocity and pressure nodes, respectively. The B, D, and H submatrices contain the discretization of the implicitly treated terms, divergence operator, and gradient operator, respectively.

The discretized velocity vector on each component grid is split into two parts. Each component grid will be composed of some nodes that are time advanced using the Navier–Stokes equations, and others that are obtained by interpolation from another component grid. Nodes that are obtained by interpolation will be referred to as pseudoboundary nodes since they are located on or outside boundaries of the component grids that are not physical boundaries of the flow domain, as illustrated in Fig. 1. The discretized pressure on each component grid is also split into two parts since pseudoboundary values of pressure may be required, depending on the grid scheme and spatial discretization. The pseudoboundary nodes of the solution vector in Eq. (29) are denoted with an extra b subscript.

The update equations for the pseudoboundary nodes are simple interpolation relationships. For example, $\mathbf{u}_{1b}^n = C_1 \mathbf{u}_2^n$ and $\delta p_{2b}^n = E_2 \delta p_1^n$. The update equations for the other nodes include the discretizations of the terms in the incompressible Navier–Stokes equations. The differencing stencils used to evaluate the terms will include contributions from pseudoboundary nodes. For this reason, each of the discretization submatrices (B, D, and H) on each component grid is split into two parts to include the contributions to the equations from both interior and pseudoboundary nodes.

In addition to pseudoboundary nodes, Fig. 1 shows that component grids may also contain hole nodes which are removed from the solution vector since they are in physical locations where other component grids are used to determine the solution. Algorithmic details on the classification of the nodes in an overset grid system can be found in [2]. Note that here we do not allow pseudoboundary nodes on one component grid to be interpolated using pseudoboundary nodes from another component grid. This imposes a component grid overlap requirement based on the width of the interpolation stencil.

$$\begin{bmatrix} I & 0 & 0 & -C_1 & 0 & 0 & 0 & 0 \\ B_{1b} & B_1 & 0 & 0 & H_{1b} & H_1 & 0 & 0 \\ 0 & -C_2 & I & 0 & 0 & 0 & 0 & 0 \\ 0 & 0 & B_{2b} & B_2 & 0 & 0 & H_{2b} & H_2 \\ 0 & 0 & 0 & 0 & I & 0 & 0 & -E_1 \\ D_{1b} & D_1 & 0 & 0 & 0 & 0 & 0 & 0 \\ 0 & 0 & 0 & 0 & 0 & -E_2 & I & 0 \\ 0 & 0 & D_{2b} & D_2 & 0 & 0 & 0 & 0 \end{bmatrix} \begin{bmatrix} \mathbf{u}_{1b}^n \\ \mathbf{u}_1^n \\ \mathbf{u}_{2b}^n \\ \mathbf{u}_2^n \\ \delta p_{1b}^n \\ \delta p_1^n \\ \delta p_{2b}^n \\ \delta p_2^n \end{bmatrix} = \begin{bmatrix} 0 \\ \mathbf{r}_1^{n-1} \\ 0 \\ \mathbf{r}_2^{n-1} \\ 0 \\ 0 \\ 0 \\ 0 \end{bmatrix} + \begin{bmatrix} bc's \\ bc's \\ bc's \\ bc's \\ bc's \\ bc's \\ bc's \\ bc's \end{bmatrix}. \tag{29}$$

If the time advancement algorithm of Eq. (8) is applied on both component grids, then the submatrices for component grid 1 in Eq. (29) are

$$B_{1b} = -\beta_k \Delta t M_{1b}, \tag{30}$$

$$B_1 = I - \beta_k \Delta t M_1, \tag{31}$$

$$H_{1b} = 2\beta_k \Delta t G_{1b}, \tag{32}$$

$$H_1 = 2\beta_k \Delta t G_1, \tag{33}$$

and similar relationships hold for the component grid 2 submatrices.

2.2.1. *Block LU Decomposition*

The goal in the development of the fractional-step method on a single grid was to avoid solving the fully coupled velocity–divergence system simultaneously. The same goal holds for the development of the fractional-step method for an overset grid system, which is more complex than the single-grid system due to the coupling between component grids. We wish to perform a block LU decomposition of the matrix A in Eq. (29). In order to perform the decomposition, consider the matrix A':

$$A' = \begin{bmatrix} I & 0 & 0 & -C_1 & 0 & 0 & 0 & 0 \\ B_{1b} & B_1 & 0 & 0 & B_1H_{1b} & B_1H_1 & B_{1b}C_1H_{2b} & B_{1b}C_1H_2 \\ 0 & -C_2 & I & 0 & 0 & 0 & 0 & 0 \\ 0 & 0 & B_{2b} & B_2 & B_{2b}C_2H_{1b} & B_{2b}C_2H_1 & B_2H_{2b} & B_2H_2 \\ 0 & 0 & 0 & 0 & I & 0 & 0 & -E_1 \\ D_{1b} & D_1 & 0 & 0 & 0 & 0 & 0 & 0 \\ 0 & 0 & 0 & 0 & 0 & -E_2 & I & 0 \\ 0 & 0 & D_{2b} & D_2 & 0 & 0 & 0 & 0 \end{bmatrix}. \quad (34)$$

This differs from A only in the upper right quadrant. As was the case for the single-grid algorithm, the pressure gradient terms in the momentum equations using the modified system matrix, A', are different from those using the original system matrix, A. In particular, the submatrices that include the contribution to the momentum equation on one component grid from the pressure gradient on the other component grid are now nonzero. Using the time advancement algorithm in Eq. (8), it is easy to show that the modifications to the system of equations due to the substitution of A' for A are $\mathcal{O}(\Delta t^3)$. Therefore, the temporal order of accuracy is unchanged by the substitution of A' for A. Other choices of second-order implicit/explicit time advancement schemes will permit the same substitution. In the fully explicit case where $B_1 = B_2 = I$ and $B_{1b} = B_{2b} = 0$, A and A' are identical and the temporal order of accuracy of the explicit scheme is maintained.

A block LU decomposition of the matrix A' can be performed where

$$L = \begin{bmatrix} I & 0 & 0 & -C_1 & 0 & 0 & 0 & 0 \\ B_{1b} & B_1 & 0 & 0 & 0 & 0 & 0 & 0 \\ 0 & -C_2 & I & 0 & 0 & 0 & 0 & 0 \\ 0 & 0 & B_{2b} & B_2 & 0 & 0 & 0 & 0 \\ 0 & 0 & 0 & 0 & I & 0 & 0 & -E_1 \\ D_{1b} & D_1 & 0 & 0 & -D_1H_{1b} & -D_1H_1 & -D_{1b}C_1H_{2b} & -D_{1b}C_1H_2 \\ 0 & 0 & 0 & 0 & 0 & -E_2 & I & 0 \\ 0 & 0 & D_{2b} & D_2 & -D_{2b}C_2H_{1b} & -D_{2b}C_2H_1 & -D_2H_{2b} & -D_2H_2 \end{bmatrix} \quad (35)$$

and

$$U = \begin{bmatrix} I & 0 & 0 & 0 & 0 & 0 & C_1H_{2b} & C_1H_2 \\ 0 & I & 0 & 0 & H_{1b} & H_1 & 0 & 0 \\ 0 & 0 & I & 0 & C_2H_{1b} & C_2H_1 & 0 & 0 \\ 0 & 0 & 0 & I & 0 & 0 & H_{2b} & H_2 \\ 0 & 0 & 0 & 0 & I & 0 & 0 & 0 \\ 0 & 0 & 0 & 0 & 0 & I & 0 & 0 \\ 0 & 0 & 0 & 0 & 0 & 0 & I & 0 \\ 0 & 0 & 0 & 0 & 0 & 0 & 0 & I \end{bmatrix}. \quad (36)$$

2.2.2. *Solution Procedure*

Now that we have the LU decomposition of A', we can solve $A'\mathbf{x} = \mathbf{b}$ in two steps, $L\tilde{\mathbf{x}} = \mathbf{b}$ and $U\mathbf{x} = \tilde{\mathbf{x}}$. The solution of $L\tilde{\mathbf{x}} = \mathbf{b}$ can be decomposed into the solution of two systems. First the momentum equations are used to obtain an intermediate velocity field, $\tilde{\mathbf{u}}^n$,

$$\begin{bmatrix} I & 0 & 0 & -C_1 \\ B_{1b} & B_1 & 0 & 0 \\ 0 & -C_2 & I & 0 \\ 0 & 0 & B_{2b} & B_2 \end{bmatrix} \begin{bmatrix} \tilde{\mathbf{u}}_{1b}^n \\ \tilde{\mathbf{u}}_1^n \\ \tilde{\mathbf{u}}_{2b}^n \\ \tilde{\mathbf{u}}_2^n \end{bmatrix} = \begin{bmatrix} 0 \\ \mathbf{r}_1^{n-1} \\ 0 \\ \mathbf{r}_2^{n-1} \end{bmatrix} + \begin{bmatrix} bc's \\ bc's \\ bc's \\ bc's \end{bmatrix}, \tag{37}$$

and the change in the pressure field, $\delta\tilde{p}^n$, is then obtained using the intermediate velocity field:

$$\begin{bmatrix} -I & 0 & 0 & E_1 \\ D_1 H_{1b} & D_1 H_1 & D_{1b} C_1 H_{2b} & D_{1b} C_1 H_2 \\ 0 & E_2 & -I & 0 \\ D_{2b} C_2 H_{1b} & D_{2b} C_2 H_1 & D_2 H_{2b} & D_2 H_2 \end{bmatrix} \begin{bmatrix} \delta\tilde{p}_{1b}^n \\ \delta\tilde{p}_1^n \\ \delta\tilde{p}_{2b}^n \\ \delta\tilde{p}_2^n \end{bmatrix}$$

$$= \begin{bmatrix} 0 & 0 & 0 & 0 \\ D_{1b} & D_1 & 0 & 0 \\ 0 & 0 & 0 & 0 \\ 0 & 0 & D_{2b} & D_2 \end{bmatrix} \begin{bmatrix} \tilde{\mathbf{u}}_{1b}^n \\ \tilde{\mathbf{u}}_1^n \\ \tilde{\mathbf{u}}_{2b}^n \\ \tilde{\mathbf{u}}_2^n \end{bmatrix} - \begin{bmatrix} bc's \\ bc's \\ bc's \\ bc's \end{bmatrix}. \tag{38}$$

The solution of $U\mathbf{x} = \tilde{\mathbf{x}}$ sets $\delta p^n = \delta\tilde{p}^n$ and projects the intermediate velocity field to a divergence-free subspace:

$$\begin{bmatrix} \mathbf{u}_{1b}^n \\ \mathbf{u}_1^n \\ \mathbf{u}_{2b}^n \\ \mathbf{u}_2^n \end{bmatrix} = \begin{bmatrix} \tilde{\mathbf{u}}_{1b}^n \\ \tilde{\mathbf{u}}_1^n \\ \tilde{\mathbf{u}}_{2b}^n \\ \tilde{\mathbf{u}}_2^n \end{bmatrix} - \begin{bmatrix} 0 & 0 & C_1 H_{2b} & C_1 H_2 \\ H_{1b} & H_1 & 0 & 0 \\ C_2 H_{1b} & C_2 H_1 & 0 & 0 \\ 0 & 0 & H_{2b} & H_2 \end{bmatrix} \begin{bmatrix} \delta p_{1b}^n \\ \delta p_1^n \\ \delta p_{2b}^n \\ \delta p_2^n \end{bmatrix}. \tag{39}$$

Finally, the pressure field is updated using the computed pressure change, δp^n. Note that the steps associated with Eqs. (37)–(39) are identical to the steps in the single-grid fractional-step method, but the details of the coupling between component grids are now represented.

2.3. Overset Grid Method Implementation

To investigate implementation details of the fractional-step method on overset grids we consider component grids using a staggered grid arrangement of the dependent variables and second-order-accurate finite-volume flux differencing. In addition to the well-established conservation properties of this choice of grid scheme and discretization, all pressure nodes are in the interior of the domain. Therefore, pressure boundary conditions are not required at the physical boundaries of the flow domain.

2.3.1. *Momentum Update*

The solution of Eq. (37) may be quite complicated depending on the number of component grids and the coupling between them. However, it may not be necessary to use implicit time advancement on all the component grids. Consider the case of flow over a cylinder where the overset grid is composed of a background Cartesian grid and a cylindrical grid to resolve the flow near the surface of the cylinder. In this case, implicit time advancement would be desirable on the cylindrical grid to alleviate the time-step restriction, but explicit time advancement could be used for the background Cartesian grid. If component grid 1 were treated fully explicitly, then $B_{1b} = 0$ and $B_1 = I$ in Eq. (37), which allows for the solution of $\tilde{\mathbf{u}}_1^n$ without any information from component grid 2 at time level n. $\tilde{\mathbf{u}}_{2b}^n$ is then determined by interpolation of $\tilde{\mathbf{u}}_1^n$, and $\tilde{\mathbf{u}}_2^n$ can then be computed. Finally, $\tilde{\mathbf{u}}_{1b}^n$ is determined by interpolation of $\tilde{\mathbf{u}}_2^n$. The momentum update is always decoupled in this way if explicit time advancement is used on all component grids.

2.3.2. *Poisson Solve*

The solution of Eq. (38) corresponds to a fully coupled Poisson solve for the pressure field. One benefit of using second-order-accurate finite-volume flux differencing on a staggered grid system is that there are no pressure pseudoboundary nodes. This reduces Eq. (38) to a more manageable system:

$$\begin{bmatrix} D_1 H_1 & D_{1b} C_1 H_2 \\ D_{2b} C_2 H_1 & D_2 H_2 \end{bmatrix} \begin{bmatrix} \delta \tilde{p}_1^n \\ \delta \tilde{p}_2^n \end{bmatrix} = \begin{bmatrix} D_{1b} & D_1 & 0 & 0 \\ 0 & 0 & D_{2b} & D_2 \end{bmatrix} \begin{bmatrix} \tilde{\mathbf{u}}_{1b}^n \\ \tilde{\mathbf{u}}_1^n \\ \tilde{\mathbf{u}}_{2b}^n \\ \tilde{\mathbf{u}}_2^n \end{bmatrix} - \begin{bmatrix} bc's \\ bc's \end{bmatrix}. \tag{40}$$

Here there is no ambiguity regarding the pressure boundary conditions at the pseudoboundaries of the component grids. Other authors using pressure projection methods on overset grid systems have chosen a pressure pseudoboundary condition based on physical reasoning or convenience. Hinatsu and Ferziger [6] argued that either Dirichlet or Neumann boundary conditions could be used but they chose Neumann boundary conditions because they were easier to implement and gave faster convergence in the multigrid solution of the equation for the pressure. Perng and Street [13] concluded that Dirichlet boundary conditions could be used in cases where the nodes from the component grids overlapped exactly, but Neumann boundary conditions should be used when the nodes do not overlap exactly. The matrix factorization used here makes the choice of the pressure pseudoboundary condition unnecessary. The off-diagonal coupling submatrices in Eq. (40), $D_{1b} C_1 H_2$ and $D_{2b} C_2 H_1$, clearly connect the pressure fields on the component grids through the interpolation of the pressure gradient.

Though it is possible to assemble the matrix and solve Eq. (40) directly, here we choose to solve the system with an iterative scheme. In this case, the off-diagonal coupling terms are moved to the right hand side and the equations for each component grid are solved independently. Consider the iterative solution of the equation for the pressure change on component grid 1,

$$D_1 H_1 \delta \tilde{p}_1^n = D_{1b} \tilde{\mathbf{u}}_{1b}^n + D_1 \tilde{\mathbf{u}}_1^n - D_{1b} C_1 H_2 \delta \tilde{p}_2^n - bc's, \tag{41}$$

where $\delta\tilde{p}_2^n$ is the current estimate for the solution on component grid 2 and $\delta\tilde{p}_1^n$ will be the new estimate for the solution on component grid 1. The matrix D_1H_1 is singular since the pressure is only known up to a constant. A standard technique to remove the singularity is to replace one of the equations with an equation that sets the level of the pressure [6]. This technique is valid as long as the replaced equation in the original system can be written as a linear combination of the other equations. We know that summing the rows of D_1H_1 produces a row of zeroes because of the telescoping property of the finite-volume flux differencing used to construct D_1. However, there is no guarantee that the sum of the right hand sides of Eq. (41) is zero because part of the right hand side comes from interpolation of the gradient of $\delta\tilde{p}_2^n$ and the interpolation of the intermediate velocity field on component grid 2. Therefore, we cannot replace one of the equations, or the solution will not satisfy the equation that was replaced in the original system (leading to a large divergence in one cell after projection).

The requirement that the sum of the right hand sides is zero is analogous to the solvability condition for Laplace's equation with zero Neumann boundary conditions. To satisfy this solvability condition for our system, the right hand side must be adjusted so that the sum is zero. Once the system is solvable, one of the equations can be replaced to set the level of the pressure and the system is no longer singular.

There is no unique way to perform the right hand side adjustment. The obvious procedure is to subtract a fraction of the sum of the right hand sides from each equation such that the sum of the new right hand sides is zero. This adjustment introduces an error into each equation which leads to a nonzero divergence in each cell after projection. If a uniform adjustment, q_1, is subtracted from the right hand side of every equation in Eq. (41) then the discrete continuity equation for component grid 1 in Eq. (29) is replaced by

$$D_{1b}\mathbf{u}_{1b}^n + D_1\mathbf{u}_1^n = q_1 + bc's. \tag{42}$$

A similar adjustment will be made during the iterative solution of $\delta\tilde{p}_2^n$. This leads to a different nonzero divergence, q_2, on component grid 2 after projection.

The fraction of the sum of the right hand sides used as an adjustment does not have to be the same in every equation. Our divergence operator was assembled using finite-volume techniques. Therefore, the nonzero divergence that results by subtracting a constant from each of the right hand sides in Eq. (41) is volume weighted. On a uniform Cartesian grid, the divergence will be the same everywhere, but on a uniform cylindrical grid, the divergence will depend on radial location. However, a volume-weighted adjustment to the right hand side of Eq. (41) can be chosen to produce a constant divergence on the cylindrical grid after projection. Alternatively, the adjustment could be weighted so that the divergence of the solution is smaller in specific regions of interest in the flow domain.

The adjustments, q_1 and q_2, vary in time due to changes in the flow field and changes in the interpolation conditions if the component grids are moving relative to one another. These adjustments are tied to the interpolation of quantities used in the construction of the right hand side for the Poisson solve. However, they are not tied to the incompatibility of the discrete operators. Morinishi *et al.* [12] have shown that the conservation properties of various grid schemes and discretizations are dependent on the discrete divergence. From a conservation standpoint, the discrete divergence should be as small as possible. Therefore, it is advantageous to only have the interpolation conditions contributing to the discrete divergence.

The previous discussion applies directly to an iterative solution of Eq. (40). A different procedure may be necessary for an iterative solution of Eq. (38), depending on the grid scheme and discretization. In the case where the Poisson solve for all grids is done simultaneously as one system of equations, Henshaw [5] suggests solving an augmented system that is nonsingular.

2.3.3. *Initial Condition*

The initial condition for Eq. (29) should be divergence free. Provided that the normal component of the velocity on the physical boundary of the flow domain satisfies global-mass conservation, the velocities in the interior of the domain can be projected using the standard technique [5]. Given an initial condition that is not divergence free, $\tilde{\mathbf{u}}^0$, we define a new initial condition, $\mathbf{u}^0$:

$$\begin{aligned} \mathbf{u}_1^0 &= \tilde{\mathbf{u}}_1^0 - G_1\phi_1 \\ \mathbf{u}_2^0 &= \tilde{\mathbf{u}}_2^0 - G_2\phi_2 \\ \mathbf{u}_{1b}^0 &= C_1\mathbf{u}_2^0 \\ \mathbf{u}_{2b}^0 &= C_2\mathbf{u}_1^0. \end{aligned} \tag{43}$$

By applying the discrete continuity equation to Eq. (43), we obtain a system of equations for ϕ:

$$\begin{bmatrix} D_1G_1 & D_{1b}C_1G_1 \\ D_{2b}C_2G_1 & D_2G_2 \end{bmatrix} \begin{bmatrix} \phi_1 \\ \phi_2 \end{bmatrix} = \begin{bmatrix} D_1 & D_{1b}C_1 \\ D_{2b}C_2 & D_2 \end{bmatrix} \begin{bmatrix} \tilde{\mathbf{u}}_1^0 \\ \tilde{\mathbf{u}}_2^0 \end{bmatrix} + \begin{bmatrix} bc's \\ bc's \end{bmatrix}. \tag{44}$$

The solution of Eq. (44) can be obtained the same way as the solution of Eq. (40). However, the projected initial condition will not be divergence free for the same reason that the time-advanced velocity field is not divergence free.

2.3.4. *Interpolation Equations*

Chesshire and Henshaw [2] have shown that third-order-accurate interpolation is required to maintain second-order accuracy in the solution of second-order elliptic equations on an overset grid. Therefore, quadratic interpolation is used to determine the interpolation submatrices in Eq. (29). Though we can achieve the same spatial order of accuracy as a single-grid solution with our overset grid solution, the discrete continuity equation cannot be satisfied in the overset grid case due to the interpolation, as discussed previously. However, it is possible to make a correction to the interpolation submatrices so that discrete continuity will be satisfied for the overset grid solution.

If the boundary of a component grid is made up of N nodes, where N_1 are physical boundary nodes and the remaining nodes are pseudoboundary nodes, then any $\mathbf{u}\,(x, y, z, t)$ that satisfies Eqs. (1) and (2) will also satisfy the discrete integral of the continuity equation over the component grid to second-order accuracy:

$$\sum_{l=1}^{N} \tilde{u}_l\, dS_l = \sum_{l=1}^{N_1} \tilde{u}_l\, dS_l + \sum_{l=N_1+1}^{N} \tilde{u}_l\, dS_l = \mathcal{O}\big(\Delta_x^2, \Delta_y^2, \Delta_z^2\big). \tag{45}$$

Here $\tilde{u}_l$ is the normal component of $\mathbf{u}$ at the boundary nodes and dS_l is the discrete normal area associated with the boundary node. Since the truncation error associated with the interpolation at the pseudoboundary nodes is third order, we can rewrite the pseudoboundary portion of the summation in Eq. (45) using the interpolated values, $\tilde{u}^*_l$ (assuming that the grid spacing on the boundary of the component grid is similar to the grid spacing used in interpolating to the pseudoboundary nodes). We then define new interpolated values of the normal component of velocity, $\tilde{u}'_j$, at the pseudoboundary nodes,

$$\tilde{u}'_j = \tilde{u}^*_j - \frac{1}{S^*}\left[\sum_{l=1}^{N_1} \tilde{u}_l \, dS_l + \sum_{l=N_1+1}^{N} \tilde{u}^*_l \, dS_l\right] = \tilde{u}^*_j + \mathcal{O}\big(\Delta_x^2, \Delta_y^2, \Delta_z^2\big), \tag{46}$$

where S^* is the total discrete normal area associated with the pseudoboundary nodes on the component grid. Using these new interpolated values, the discrete integral of the continuity equation over the component grid is satisfied to machine accuracy:

$$\sum_{j=1}^{N_1} \tilde{u}_j \, dS_j + \sum_{j=N_1+1}^{N} \tilde{u}'_j \, dS_j = 0. \tag{47}$$

Now consider the sum of the right hand sides of Eq. (41). Due to the telescoping properties of the discrete divergence operator, D_1, only the interpolated term $D_{1b}(\hat{\mathbf{u}}^{n}_{1b} - C_1 H_2 \delta \hat{P}^n_2)$ and the boundary conditions contribute to the summation. The summation then becomes the discrete integral of the normal component of velocity over the boundary of the component grid. We have shown in Eq. (47) that the discrete integral of the normal component of the velocity is zero for the corrected interpolation weights. This guarantees that the sum of the right hand sides for the Poisson solve on the component grid will be zero. Therefore, the right hand sides do not need to be adjusted and the discrete continuity equation will be satisfied to machine accuracy after projection.

If the modified interpolation weights are used then the discrete continuity equation is satisfied to machine accuracy and the conservation properties of the second-order-accurate, staggered grid scheme on each component grid are maintained [12]. However, conservation is not achieved at the interfaces between the component grids. Chesshire and Henshaw [3] have shown how to derive conservative interpolation weights for the solution of conservation laws on overset grid systems. Their method treats both the interpolation weights for the fluxes and the weights in the numerical approximation of the integral of the conserved quantity as free parameters that are solved for as part of an overdetermined system of equations. Wright and Shyy [17] have developed a conservative interpolation scheme for the solution of the incompressible Navier–Stokes equations based on linear interpolation of mass and momentum fluxes. Since the derivation of our overset grid fractional-step method requires that the velocity components are interpolated instead of the fluxes, we do not consider conservative interpolation in this work. A good review of work on interface treatments and discussion of conservative treatments for multiblock calculations can be found in the paper by Liu and Shyy [10].

The correction to the interpolation equations for the normal component of velocity at pseudoboundary nodes can be used to define a new interpolation submatrix in Eq. (29). Equation (46) shows that the truncation error associated with the corrected interpolation weights is second order. Therefore, we will not maintain second-order spatial accuracy if we use the corrected interpolation weights. If a set of third-order-accurate interpolation weights can be found such that Eq. (47) is satisfied, then the spatial order of accuracy can be maintained along with the conservation properties of the staggered grid scheme. In this work we will use the noncorrected interpolation weights so that the second-order spatial accuracy is maintained.

3. NUMERICAL RESULTS

To verify that the predicted spatial and temporal orders of accuracy are maintained, the overset grid fractional-step method was applied to two-dimensional unsteady problems. The spatial order of accuracy was validated using the Taylor vortex array. The temporal order of accuracy was validated using flow over a circular cylinder at $Re = 100$.

3.1. Spatial Order of Accuracy

The Taylor vortex array is an analytical solution to the two-dimensional, incompressible Navier–Stokes equations. For $Re = 1$ (based on the maximum initial velocity and the domain length divided by 2π), the solution is

$$\begin{aligned} u(x, y, t) &= -\cos x \sin y \exp(-2t) \\ v(x, y, t) &= \sin x \cos y \exp(-2t) \\ p(x, y, t) &= -\frac{1}{4}(\cos 2x + \cos 2y) \exp(-4t). \end{aligned} \tag{48}$$

We solved this problem using an overset grid similar to the one shown in Fig. 1. The grid points shown in Fig. 1 represent the cell-centered pressure nodes of the staggered grid system. Since there are no pseudoboundary pressure nodes for our grid scheme and discretization, the pseudoboundary nodes marked in Fig. 1 correspond to the centers of the cells along the boundary of the inner grid and also along the hole boundary of the background grid. Interpolation of the velocity occurs at the boundaries of these cells for the normal component and half a grid cell outside the boundaries of these cells for the tangential component, as dictated by the staggered grid arrangement of the dependent variables.

The computational domain is $[x_1, x_2] \times [y_1, y_2] = [0, 2\pi] \times [0, 2\pi]$ with periodic boundary conditions. The code is set up to allow the centered inner grid to be rotated to any angle relative to the background grid. The dimensions of the inner grid are half of the corresponding background grid dimensions. As discussed previously, there is a minimum overlap required to ensure that pseudoboundary nodes are not used for interpolation to another component grid. We first identify the background grid nodes used for interpolation to the inner grid and then choose the background grid hole and pseudoboundary nodes to satisfy the minimum overlap requirement. Another way to choose the overlap is to mark background grid nodes inside a specified spatial region as hole nodes and then identify the background grid pseudoboundary nodes. This fixed overlap must be at least as large as the minimum overlap. If minimum overlap is specified then the size of the overlap will shrink during grid refinement and the hole boundary will approach the inner grid boundary. Fixed overlap will cause the hole boundary to stay in the same location during grid refinement although small changes may occur due to improved resolution of the specified hole region by the background grid.

To fully investigate the spatial order or accuracy of our fractional-step overset grid scheme we considered the four cases shown in Table I. One of the benefits of the Taylor vortex array

TABLE I
Taylor Vortex Grid and Flow Configuration Cases

Case	Inner grid angle	Vortex shift
I	15°	(0, 0)
II	15°	$\left(\frac{\pi}{4}, \frac{\pi}{4}\right)$
III	15°	$\left(\frac{\pi}{2}, \frac{\pi}{2}\right)$
IV	45°	$\left(\frac{\pi}{2}, \frac{\pi}{2}\right)$

as a test problem is that we can easily shift the vortices and expose the background grid hole boundary to different flow conditions. We performed a grid refinement study for each case with both fixed and minimum overlap. The hole region in the background grid for each fixed-overlap case was chosen to satisfy the minimum overlap requirement for the coarsest grid, thereby satisfying the minimum overlap requirement for the finer grids. A sequence of four overset grids was used for each grid refinement study: $(24 \times 24) \cup (16 \times 16)$, $(48 \times 48) \cup (32 \times 32)$, $(96 \times 96) \cup (64 \times 64)$, and $(192 \times 192) \cup (128 \times 128)$, where the background grid is listed first.

We computed each solution until $t = 1.0$ using the same time step for all grids and the time advancement algorithm shown in Eq. (8). The initial condition was set to the analytical solution shown in Eq. (48) and then projected using the solution to Eq. (44). The viscous terms on the inner grid were treated implicitly while the other terms and all the terms on the background grid were treated explicitly. The coupled Poisson equation was solved with an alternating Schwarz method using an agglomeration multigrid algorithm [11] on each component grid and an acceleration parameter [6] to reduce the number of outer iterations.

Time histories of the root mean square (rms) error in the computed u component of the velocity on the inner grid for fixed overlap are shown in Fig. 3. In all four cases, the error histories show second-order spatial accuracy. Similar plots for minimum overlap computations are shown in Fig. 4. The spatial order of accuracy is clearly degraded for the minimum overlap computations except for case IV. The degradation of the spatial order of accuracy for the minimum overlap simulations appears to be inconsistent with the analytical work of Chesshire and Henshaw [2] on the interpolation order of accuracy required to maintain the overall spatial order of accuracy. In order to investigate this inconsistency, we consider the steady, incompressible Stokes equations in two dimensions. To reduce the complexity of the analysis, we perform a Fourier transform on the equations in the y-direction:

$$\begin{aligned}\frac{\partial \hat{p}}{\partial x} &= \frac{\partial^2 \hat{u}}{\partial x^2} - k^2 \hat{u}\\ ik\hat{p} &= \frac{\partial^2 \hat{v}}{\partial x^2} - k^2 \hat{v}\\ 0 &= \frac{\partial \hat{u}}{\partial x} + ik\hat{v}.\end{aligned} \tag{49}$$

Now that the problem has been reduced to a one-dimensional system of equations with a parameter, k, we discretize Eq. (49) on the overset, staggered grid shown in Fig. 5. The physical boundaries of the computational domain are located at Xx_0^1 and $\mathrm{Xx}_{N_2}^2$. The

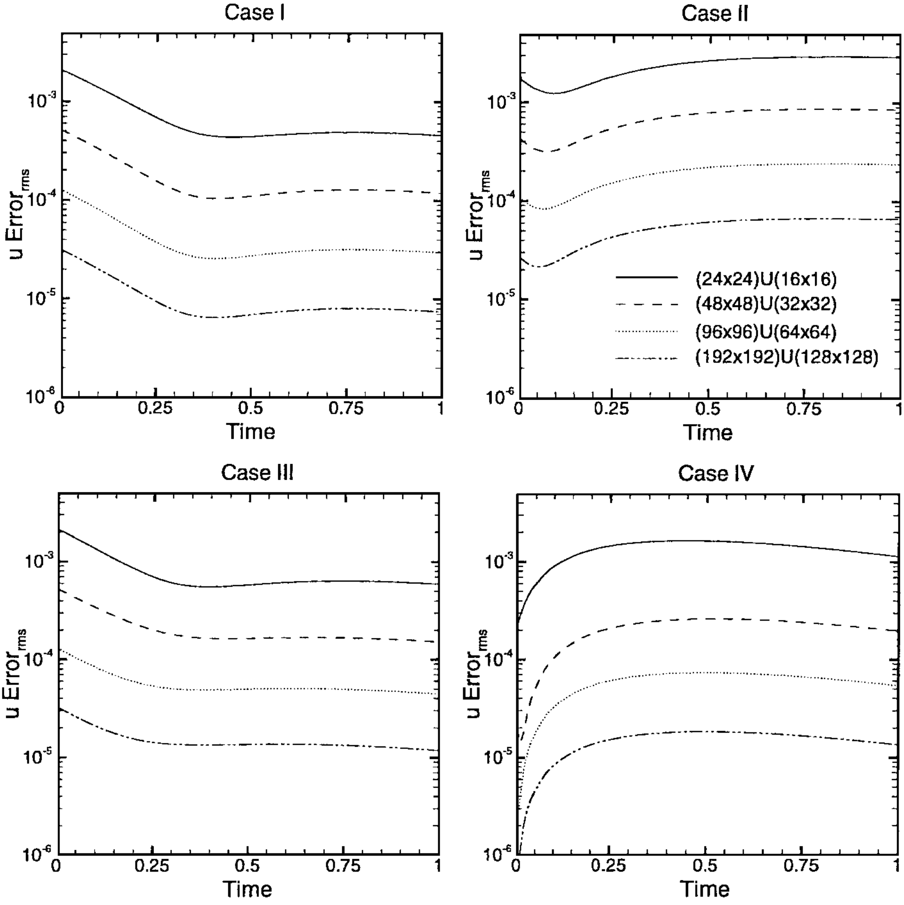

FIG. 3. Taylor vortex u velocity component rms error histories on inner grid. Fixed overlap grid refinement study.

discretized $\hat{u}$ component of velocity is stored at the Xx locations and the discretized $\hat{v}$ component and pressure are stored at the Xy locations. The $\hat{u}$ pseudoboundary nodes are located at $\mathrm{Xx}^1_{N_1}$ and Xx^2_0 on component grids 1 and 2, respectively. The $\hat{v}$ pseudoboundary nodes are located at $\mathrm{Xy}^1_{N_1+1}$ and Xy^2_0 on component grids 1 and 2, respectively. In Fig. 5 there is sufficient overlap so that pseudoboundary nodes are not used for quadratic interpolation to the other component grid, as dictated by our formulation. If higher order interpolation is used then the required component grid overlap will become larger.

We apply second-order-accurate finite differences to Eq. (49) to obtain the set of discrete equations on each component grid:

$$\frac{\hat{p}^l_{j+1}-\hat{p}^l_j}{\Delta x_l} = \frac{\hat{u}^l_{j+1}-2\hat{u}^l_j+\hat{u}^l_{j-1}}{\Delta x_l^2} - k^2\hat{u}^l_j \quad \text{for } j = 1:N_l-1, \tag{50}$$

$$ik\hat{p}^l_j = \frac{\hat{v}^l_{j+1}-2\hat{v}^l_j+\hat{v}^l_{j-1}}{\Delta x_l^2} - k^2\hat{v}^l_j \quad \text{for } j = 1:N_l, \tag{51}$$

$$\delta^l_{k,0} = \frac{\hat{u}^l_j-\hat{u}^l_{j-1}}{\Delta x_l} + ik\hat{v}^l_j \quad \text{for } j = 1:N_l. \tag{52}$$

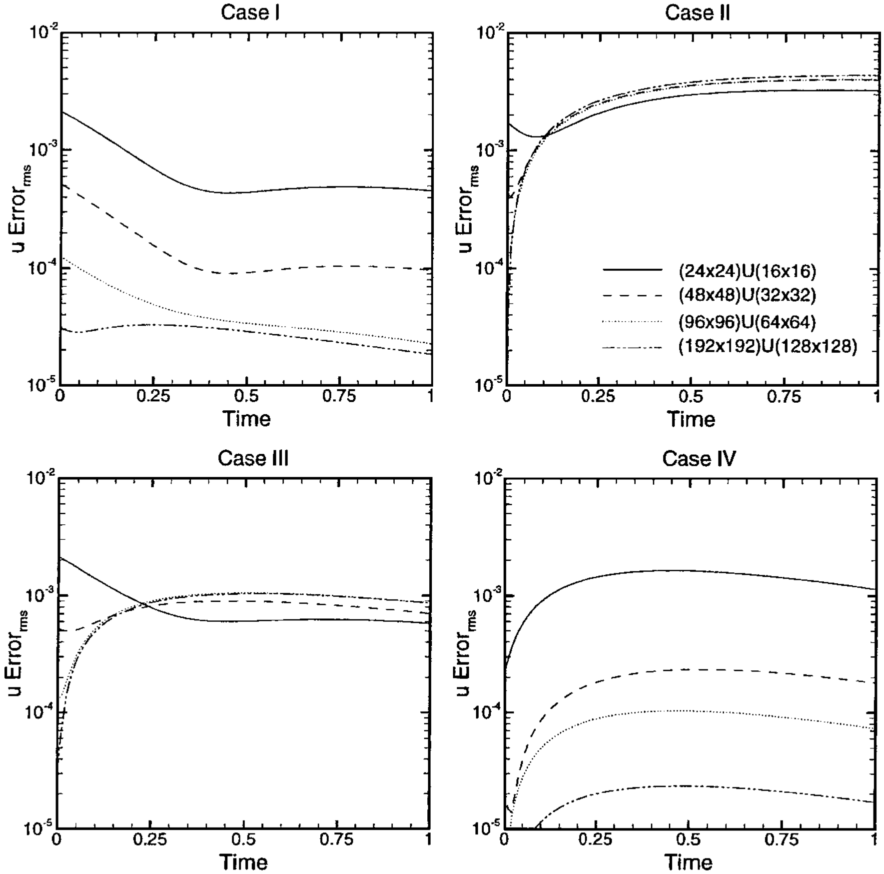

FIG. 4. Taylor vortex *u* velocity component rms error histories on inner grid. Minimum overlap grid refinement study.

In anticipation of the correction to the right hand side of the Poisson equation that will be required to guarantee solvability, the discrete continuity equation for $k = 0$ is modified with the term $\delta^l_{k,0}$. In making this modification, we have assumed that the same correction will be applied to every equation in the Poisson solve on each component grid and that the correction is constant in the y-direction.

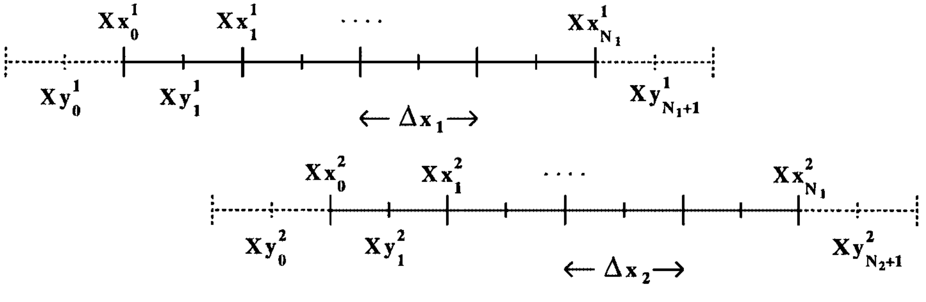

FIG. 5. One-dimensional overset staggered grid.

The discrete equations (50)–(52) are supplemented by interpolation equations for the pseudoboundary nodes,

$$\begin{aligned}\hat{u}^1_{N_1} &= \sum_{m=0}^{q-1} \alpha^1_m \hat{u}^2_{a+m}\\ \hat{v}^1_{N_1+1} &= \sum_{m=0}^{q-1} \beta^1_m \hat{v}^2_{b+m}\\ \hat{u}^2_0 &= \sum_{m=0}^{q-1} \alpha^2_m \hat{u}^1_{c+m}\\ \hat{v}^2_0 &= \sum_{m=0}^{q-1} \beta^2_m \hat{v}^1_{d+m},\end{aligned} \tag{53}$$

where q is the order of accuracy of the interpolation and α^l_m and β^l_m are interpolation weights.

We first consider the case where $k = 0$. In this case, the discrete momentum equations are decoupled from one another. The $\hat{v}$ momentum equation (51) is a second-order-accurate discretization of a second-order elliptic equation. The $\hat{u}$ momentum equation (50) is also a second-order accurate discretization of a second-order elliptic equation with the pressure gradient as a source term. The analysis of Chesshire and Henshaw [2] shows that third-order-accurate interpolation is sufficient to maintain second-order accuracy in the solution of a second-order equation if the component grid overlap shrinks during grid refinement. Results from numerical tests for $k = 0$ agree with their analysis and are not presented here.

We now consider the case where $k \neq 0$. Using Eq. (52), we can write $\hat{v}$ in terms of $\hat{u}$,

$$\hat{v}^l_j = \frac{i}{k}\frac{\hat{u}^l_j - \hat{u}^l_{j-1}}{\Delta x_l} \quad \text{for } j = 1 : N_l, \tag{54}$$

and Eq. (54) can then be used in Eq. (51) to solve for the pressure:

$$\begin{aligned}\hat{p}^l_j &= \frac{\hat{u}_{j+1} - \hat{u}_j - 2(\hat{u}^l_j - \hat{u}^l_{j-1}) + \hat{v}^l_0}{k^2 \Delta x_l^3} - \frac{\hat{u}^l_j - \hat{u}^l_{j-1}}{\Delta x_l} \quad \text{for } j = 1,\\ \hat{p}^l_j &= \frac{\hat{u}_{j+1} - \hat{u}_j - 2(\hat{u}^l_j - \hat{u}^l_{j-1}) + \hat{u}^l_{j-1} - \hat{u}^l_j}{k^2 \Delta x_l^3} - \frac{\hat{u}^l_j - \hat{u}^l_{j-1}}{\Delta x_l} \quad \text{for } j = 2 : N_l - 1,\\ \hat{p}^l_j &= \frac{\hat{v}^l_{N_l+1} - 2(\hat{u}^l_j - \hat{u}^l_{j-1}) + \hat{u}^l_{j-1} - \hat{u}^l_j}{k^2 \Delta x_l^3} - \frac{\hat{u}^l_j - \hat{u}^l_{j-1}}{\Delta x_l} \quad \text{for } j = N_l.\end{aligned} \tag{55}$$

Finally, Eq. (55) can be used in Eq. (50) to determine a new discrete equation for $\hat{u}$:

$$\begin{aligned}&\frac{\hat{u}^l_{j+2} - 4\hat{u}^l_{j+1} + 6\hat{u}^l_j - 3\hat{u}^l_{j-1} - \frac{k\Delta x_l}{i}\hat{v}^l_0}{k^2 \Delta x_l^4} - \frac{\hat{u}^l_{j+1} - 2\hat{u}^l_j + \hat{u}^l_{j-1}}{\Delta x_l^2}\\ &\quad = \frac{\hat{u}^l_{j+1} - 2\hat{u}^l_j + \hat{u}^l_{j-1}}{\Delta x_l^2} - k^2 \hat{u}^l_j \quad \text{for } j = 1,\end{aligned} \tag{56}$$

$$\begin{aligned}
&\frac{\hat{u}^l_{j+2} - 4\hat{u}^l_{j+1} + 6\hat{u}^l_j - 4\hat{u}^l_{j-1} + \hat{u}^l_{j-2}}{k^2 \Delta x_l^4} - \frac{\hat{u}^l_{j+1} - 2\hat{u}^l_j + \hat{u}^l_{j-1}}{\Delta x_l^2} \\
&\quad = \frac{\hat{u}^l_{j+1} - 2\hat{u}^l_j + \hat{u}^l_{j-1}}{\Delta x_l^2} - k^2 \hat{u}^l_j \quad \text{for } j = 2 : N_l - 2,
\end{aligned} \tag{57}$$

$$\begin{aligned}
&\frac{\frac{k\Delta x_l}{i}\hat{v}^l_{N_l+1} - 3\hat{u}^l_{j+1} + 6\hat{u}^l_j - 4\hat{u}^l_{j-1} + \hat{u}^l_{j-2}}{k^2 \Delta x_l^4} - \frac{\hat{u}^l_{j+1} - 2\hat{u}^l_j + \hat{u}^l_{j-1}}{\Delta x_l^2} \\
&\quad = \frac{\hat{u}^l_{j+1} - 2\hat{u}^l_j + \hat{u}^l_{j-1}}{\Delta x_l^2} - k^2 \hat{u}^l_j \quad \text{for } j = N_l - 1.
\end{aligned} \tag{58}$$

We now have a single discrete equation for $\hat{u}$ that is algebraically equivalent to the original system of equations for $\hat{u}$, $\hat{v}$, and $\hat{p}$. Equation (57) shows that the equation for the majority of the interior nodes on each component grid is the second-order discretization of the fourth-order equation

$$\frac{1}{k^2}\frac{\partial^4 \hat{u}}{\partial x^4} - 2\frac{\partial^2 \hat{u}}{\partial x^2} + k^2 \hat{u} = 0, \tag{59}$$

which can be derived from Eq. (49). However, Eqs. (56) and (58) for the $\hat{u}$ nodes adjacent to the boundary nodes of the component grids show a modification to the discretization of the fourth-order derivative due to the implementation of the boundary conditions in the original discretized system of Eqs. (50)–(52). We assume that the modification to the evaluation of the fourth-order derivative at a node adjacent to a physical boundary node does not affect the spatial order of accuracy of the solution since a single-grid solution of Eqs. (50)–(52) shows second-order spatial accuracy. However, the equation for a $\hat{u}$ node adjacent to a pseudoboundary node should be consistent with a second-order evaluation of Eq. (59).

On component grid 1 in Fig. 5, the fourth-order derivative term in the discrete equation for $\hat{u}$ at $\mathrm{Xx}^1_{N_1-1}$ (58) involves $\hat{v}^1_{N_1+1}$, which is interpolated from component grid 2. Using the interpolation equations (53), Eq. (54), and a Taylor series expansion, we can rewrite the term with $\hat{v}^1_{N_1+1}$ as follows:

$$\begin{aligned}
\frac{k\Delta x_1}{i}\hat{v}^1_{N_1+1} &= \frac{k\Delta x_1}{i}\sum_{m=0}^{q-1}\beta^1_m \hat{v}^2_{b+m} = \frac{\Delta x_1}{\Delta x_2}\sum_{m=0}^{q-1}\beta^1_m\left(\hat{u}^2_{b+m} - \hat{u}^2_{b+m-1}\right) \\
&= \frac{\Delta x_1}{\Delta x_2}\left(\hat{u}\left(Xy^1_{N_1+1} + \frac{\Delta x_2}{2}\right) - \hat{u}\left(Xy^1_{N_1+1} - \frac{\Delta x_2}{2}\right)\right) + \mathcal{O}\left(\Delta x_2^q\right) \\
&= \hat{u}\left(Xy^1_{N_1+1} + \frac{\Delta x_1}{2}\right) - \hat{u}\left(Xy^1_{N_1+1} - \frac{\Delta x_1}{2}\right) \\
&\quad + \frac{\left(\Delta x_1 \Delta x_2^2 - \Delta x_1^2 \Delta x_2\right)}{24}\frac{\partial^3 \hat{u}}{\partial x^3}\left(Xy^1_{N_1+1}\right) + \mathcal{O}\left(\Delta x_2^q\right) \\
&= \hat{u}^1_{N_1+1} - \hat{u}^1_{N_1} + \mathcal{O}\left(\Delta x_1 \Delta x_2^2 - \Delta x_1^2 \Delta x_2\right) + \mathcal{O}\left(\Delta x_2^q\right).
\end{aligned} \tag{60}$$

Therefore, the modified fourth-order derivative at $\mathrm{Xx}^1_{N_1-1}$ is equivalent to a standard second-order discretization at $\mathrm{Xx}^1_{N_1-1}$ using values at two interpolation points, $\mathrm{Xx}^1_{N_1}$ and $\mathrm{Xx}^1_{N_1+1}$. However, the interpolation is only third-order accurate if $\Delta x_1 \neq \Delta x_2$, as shown in Eq. (60). Note that we do not directly interpolate at $\mathrm{Xx}^1_{N_1+1}$ since that node does not exist in our original discretization. The same approach can be used to show that the modified fourth-order derivative in the equation for $\hat{u}$ at Xx_1^2 on component grid 2 is equivalent to a standard second-order discretization using values at two interpolation points, Xx_{-1}^2 and Xx_0^2.

The analysis of Chesshire and Henshaw [2] proves that third-order-accurate interpolation is sufficient to maintain second-order accuracy in the solution of a fourth-order equation if the component grid overlap is fixed. If the overlap between the component grids shrinks during grid refinement then fifth-order interpolation is required. Combining our analysis with the work of Chesshire and Henshaw [2], we predict that if $\Delta x_1 = \Delta x_2$, then the solution of Eqs. (50)–(52) will be second-order accurate for the minimum overlap case if the interpolation weights in Eq. (53) are fifth-order accurate. However, if $\Delta x_1 \neq \Delta x_2$ then only the fixed-overlap case will produce second-order accuracy due to the third-order error term in Eq. (60).

In order to test our conclusions regarding the spatial order of accuracy of the overset grid solution of Eq. (49), we solve Eqs. (50)–(52) on the domain $[0, 2\pi]$ using the overset grid in Fig. 5 with Dirichlet boundry conditions for the velocity components at the domain boundaries. The left boundary of component grid 2 is fixed in space at $x = 4\pi/5$ for all simulations. The right boundary of component grid 1 is at $x = 6\pi/5$ for the fixed-overlap simulations and is closer to the left boundary of component grid 2 for the minimum overlap simulations, as dictated by the width of the interpolation stencil. We add a forcing term to the right hand side of the momentum equations so that the analytical solution is spatially equivalent to the Taylor vortex array. The discrete equations are solved in the same manner as the time-accurate simulations of the Taylor vortex array until a steady-state solution is reached.

Errors in the numerical solution for the imaginary part of $\hat{u}$ for $k = 1$ when $\Delta x_1 = \Delta x_2$ are shown in Fig. 6. As predicted by our analysis, fifth-order interpolation weights are required to maintain the second-order accuracy of the numerical solution if the component grid overlap shrinks during grid refinement. Similar results for the case where $\Delta x_1 \neq \Delta x_2$ are shown in Fig. 7. In this case, the results show that it is not possible to achieve

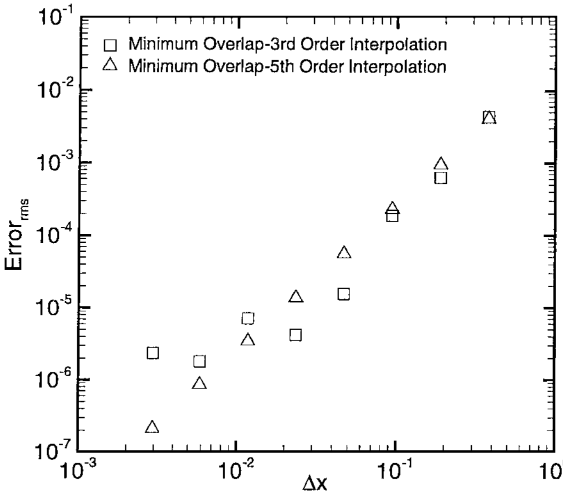

FIG. 6. $\hat{u}$ error in numerical solution of Stokes equations for $k = 1$ on a one-dimensional overset grid with $\Delta x_1 = \Delta x_2$.

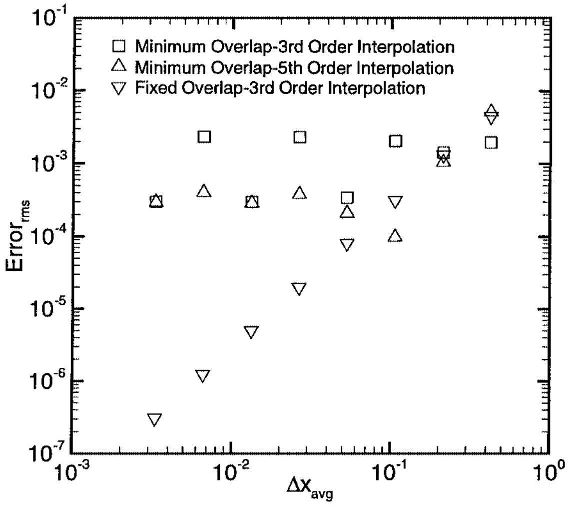

FIG. 7. $\hat{u}$ error in numerical solution of Stokes equations for $k = 1$ on a one-dimensional overset grid with $\Delta x_1 = \frac{5}{4}\Delta x_2$.

second-order spatial accuracy unless the overlap of the component grids is held fixed during grid refinement.

Analysis has shown that our discretized system of second-order equations behaves like a discretized fourth-order equation. Note that this is not an artifact of the staggered grid system. An analysis of a collocated grid solution to Eq. (49) reveals that the equivalent fourth-order discretized equation has modified terms at two nodes ajacent to a pseudoboundary node instead of the single node that occurs for the staggered grid system. This is due to the fact that the continuity equation and the pressure gradient term are discretized on cells of length $2\Delta x$ in the collocated grid discretization (leading to odd–even decoupling of the pressure field). Our analysis can easily be extended to three dimensions by considering the Stokes equations after Fourier transformations in two directions. Since the required order of interpolation in an overset grid solution is controlled by the highest order derivative in the equation, our analysis should extend directly to the Navier–Stokes equations. This conclusion is supported by the results of the time-dependent simulations of the Taylor vortex array.

Our analysis and results have shown that the overset grid fractional-step method maintains the correct spatial order of accuracy only if the overlap of the component grids is held fixed during grid refinement (except for special cases). Henshaw [5] has shown results where fourth-order spatial accuracy is maintained in the solution of the velocity–pressure formulation of the Navier–Stokes equations when the overlap shrinks during grid refinement. The difference between the results of the two approaches is due to the enforcement of the discrete continuity equation. We have shown that when the discrete continuity equation is enforced, the second-order discretization of the system of second-order equations is equivalent to a second-order discretization of a fourth-order equation, and the equivalent equations for the nodes near the pseudoboundaries lead to degradation of the spatial order of accuracy in the case of minimum overlap. In the velocity–pressure formulation, the continuity equation is replaced by an elliptic equation for the pressure, and discrete continuity is enforced only to within the truncation error of the discretization. The discretization of the velocity–pressure formulation leads to a system of second-order equations that are effectively decoupled from one another. Therefore, the analysis of Chesshire and Henshaw [5] for second-order elliptic equations can be directly applied and the correct spatial order of accuracy can be maintained in the case of minimum overlap.

3.2. Temporal Order of Accuracy

The flow over a circular cylinder at $Re = 100$ is a more complex flow, both temporally and spatially, than the Taylor vortex array. Though we do not have an analytical solution, we can still use the numerical solution to verify that the predicted temporal order of accuracy is maintained. It is important to verify the time accuracy of the numerical solution since we wish to use different time integration schemes on different component grids and we are forced to make a time-dependent adjustment to the right hand side of the discrete continuity equation.

The problem setup is similar to that in [5]. The computational domain is $[x_1, x_2] \times [y_1, y_2] = [-2.5, 15] \times [-3.5, 3.5]$ with a cylinder of radius 0.5 centered at the origin. A uniform inflow condition is applied at the left boundary and slip walls are used on the top and bottom boundaries. A convective boundary condition of the form

$$\frac{\partial \mathbf{u}}{\partial t} + U_\infty \frac{\partial \mathbf{u}}{\partial x} = 0 \tag{61}$$

is used at the right boundary. A portion of the $(175 \times 70) \cup (20 \times 64)$ grid used for this test problem is shown in Fig. 8. The background grid has a uniform grid spacing of 10 cells per cylinder diameter. The cylindrical grid extends one diameter from the cylinder surface and is stretched to resolve the flow close to the cylinder surface. The overlap is set using the minimum overlap criteria dictated by the biquadratic interpolation stencil.

The desired flow condition for the time accuracy study was the shedding cylinder. In order to reach this condition, we ran the code from an appropriately projected initial condition

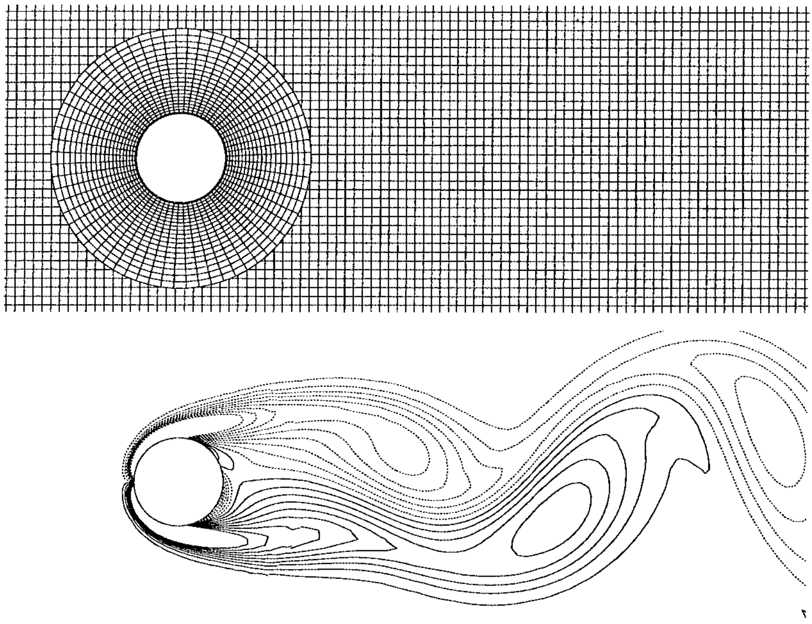

FIG. 8. Grid and vorticity contours from overset grid simulation of flow over a circular cylinder at $Re = 100$.

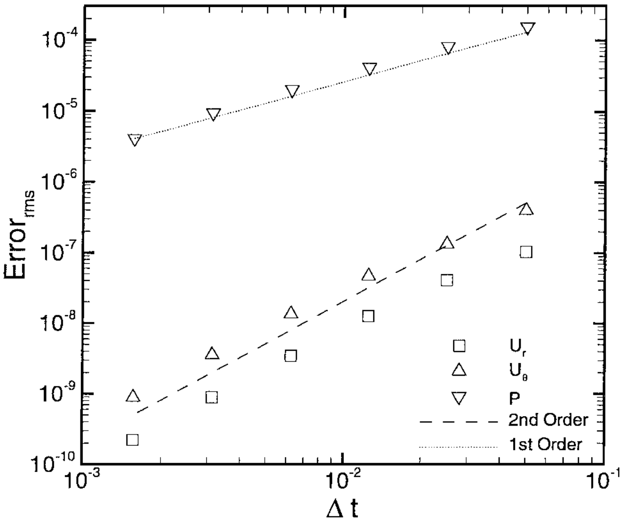

FIG. 9. Cylindrical grid time accuracy for solution of flow over a circular cylinder at $Re = 100$.

of potential flow around a cylinder using the time advancement algorithm in Eq. (8) with a variable time step. The cylindrical grid was time advanced with implicit treatment of the radial viscous terms while the background grid used fully explicit time advancement. The convective boundary condition was time advanced with third-order Runge–Kutta and the streamwise component of velocity at the right boundary was then adjusted to conserve mass. The solution of the coupled Poisson equation for the pressure was obtained using the iterative solver described in the previous section.

During time advancement, a symmetric recirculation region develops behind the cylinder and vortex shedding is eventually induced due to truncation and round-off errors in the numerical solution [8]. However, this process is extremely slow and the vortex shedding was not clearly visible in our simulations until $t = 175$. Though the delayed vortex shedding is inconvenient, it provides confidence in the quality of our numerical method. Kravchenko *et al.* [8] use B-splines and a zonal grid well suited to the solution of flow over a circular cylinder and they report that the flow at $Re = 100$ tended to stay symmetric up to $t = 200$. Vorticity contours from the shedding cylinder simulations are shown in Fig. 8.

Starting with the shedding cylinder as an initial condition, we ran the code for a length of time close to the maximum allowable time step. In this case the cylindrical grid convective terms and explicitly treated azimuthal diffusive terms contribute equally to the time-step restriction. The number of time steps used to cover the time interval was varied from 1 to 32 and an "exact" solution was computed with 160 time steps. We then computed the rms error on the cylindrical grid between each of the solutions and the "exact" solution. The results are shown in Fig. 9. The velocity components are second-order accurate in time and the pressure is first-order accurate.

Though we do not wish to perform a detailed investigation of this flow, it is important to verify that our overset grid code produces results that are consistent with previously published studies. The computational domain and grid sizes used for the time accuracy study are too small to provide accurate measurements of the lift and drag on the cylinder. We performed additional simulations in the computational domain $[x_1, x_2] \times [y_1, y_2] =$

TABLE II
Shedding Cylinder Results

Case	$C_D^{\max}$	$C_L^{\max}$	St
Overset	1.413	0.342	0.173
Kravchenko 1	1.405	0.350	0.167
Kravchenko 13	1.314	0.314	0.164

$[-6, 15] \times [-10.5, 10.5]$ on a $(256 \times 256) \cup (96 \times 128)$ grid where the cylindrical grid extended to $r = 3$ diameters. Once vortex shedding was visible, we ran the code with a constant time step until a statistically steady flow pattern was reached. Statistics from this flow pattern along with results from [8] are shown in Table II. Kravchenko's case 1 was a simulation with a domain radius and radial grid spacing at the cylinder surface that are similar to those in our simulation while case 13 used a much larger domain and a smaller radial grid spacing at the cylinder surface. Our results differ by less than 5% when compared to Kravchenko's case 1 results and they differ by less than 10% when compared to Kravchenko's case 13 results.

4. CONCLUSIONS

We have derived a fractional-step method for overset grids using an approximate *LU* decomposition of the coupled system of discretized component grid equations. The factorization of the system of equations is independent of the grid scheme and spatial discretization and is consistent with well-established methods used for single-grid calculations. Hybrid implicit/explicit time advancement schemes can be used with different treatment of terms on different component grids to alleviate time-step restrictions. All the details of the coupling between the grids are clear from the factorization, including the coupling of the pressure fields.

A particularly simple implementation of the algorithm is possible for component grids with a staggered grid arrangement of the dependent variables and second-order-accurate finite-volume flux differencing. This implementation was tested to investigate the spatial and temporal orders of accuracy of the solution. The second-order spatial accuracy was maintained for all cases considered provided that the grid overlap was held fixed during grid refinement. The temporal order of accuracy of the overset grid solution was shown to be consistent with the implementation of the time advancement algorithm on a single grid.

ACKNOWLEDGMENTS

The authors thank Dr. Joe Oefelein and Dr. Kyle Squires for their comments and suggestions. This work was supported by the Department of Energy ASCI ASAP program under Contract B341491 from the Lawrence Livermore Laboratory. Opinions expressed in the paper are those of the authors and not those of Stanford University, the Lawrence Livermore Laboratory, or the Department of Energy.

REFERENCES

1. D. L. Brown, R. Cortez, and M. L. Minion, Accurate projection methods for the incompressible Navier–Stokes equations, *J. Comput. Phy.* **168**, 464 (2001).

2. G. Chesshire and W. D. Henshaw, Composite overlapping meshes for the solution of partial differential equations, *J. Comput. Phys.* **90**, 1 (1990).
3. G. Chesshire and W. D. Henshaw, A scheme for conservative interpolation on overlapping grids, *SIAM J. Sci. Comput.* **15**, 819 (1994).
4. J. K. Dukowicz and A. S. Dvinsky, Approximate factorization as a high order splitting for the implicit incompressible flow equations, *J. Comput. Phys.* **102**, 336 (1992).
5. W. D. Henshaw, A fourth-order accurate method for the incompressible Navier–Stokes equations on overlapping grids, *J. Comput. Phys.* **113**, 13 (1994).
6. M. Hinatsu and J. H. Ferziger, Numerical computation of unsteady incompressible flow in complex geometry using a composite multigrid technique, *Int. J. Numer. Methods Fluids* **13**, 971 (1991).
7. C. Kiris, D. Kwak, S. Rogers, and I. Chang, Computational approach for probing the flow through artificial heart devices, *ASME J. Biomech. Eng.* **119**, 452 (1997).
8. A. G. Kravchenko, Parviz Moin, and Karim Shariff, B-spline method and zonal grids for simulations of complex turbulent flows, *J. Comput. Phys.* **151**, 757 (1999).
9. M. J. Lee, B. D. Oh, and Y. B. Kim, Canonical fractional-step methods and consistent boundary conditions for the incompressible Navier–Stokes equations, *J. Comput. Phys.* **168**, 73 (2001).
10. J. Liu and W. Shyy, Assessment of grid interface treatments for multi-block incompressible viscous flow computation, *Comput. Fluids* **25**, 719 (1996).
11. D. J. Mavriplis and V. Venkatakrishnan, Agglomeration multigrid for two-dimensional viscous flows, *Comput. Fluids* **24**, 553 (1995).
12. Y. Morinishi, T. S. Lund, O. V. Vasilyev, and P. Moin, Fully conservative higher order finite difference schemes for incompressible flow, *J. Comput. Phys.* **143**, 90 (1998).
13. C. Y. Perng and R. L. Street, A coupled multigrid-domain-splitting technique for simulating incompressible flows in geometrically complex domains, *Int. J. Numer. Methods Fluids* **13**, 269 (1991).
14. J. B. Perot, An analysis of the fractional step method, *J. Comput. Phys.* **108**, 51 (1993).
15. P. R. Spalart, *Hybrid RKW3+Crank-Nicolson Scheme*. Internal report (NASA–Ames Research Center, Moffett Field, CA), 1987.
16. J. Y. Tu and L. Fuchs, Overlapping grids and multigrid methods for three-dimensional unsteady flow calculations in IC engines, *Int. J. Numer. Methods Fluids* **15**, 693 (1992).
17. J. A. Wright and W. Shyy, A pressure-based composite grid method for the Navier–Stokes equations, *J. Comput. Phys.* **107**, 225 (1993).